Faraday Discussions

Accepted Manuscript

This manuscript will be presented and discussed at a forthcoming Faraday Discussion meeting. All delegates can contribute to the discussion which will be included in the final volume.

Register now to attend! Full details of all upcoming meetings: http://rsc.li/fd-upcoming-meetings

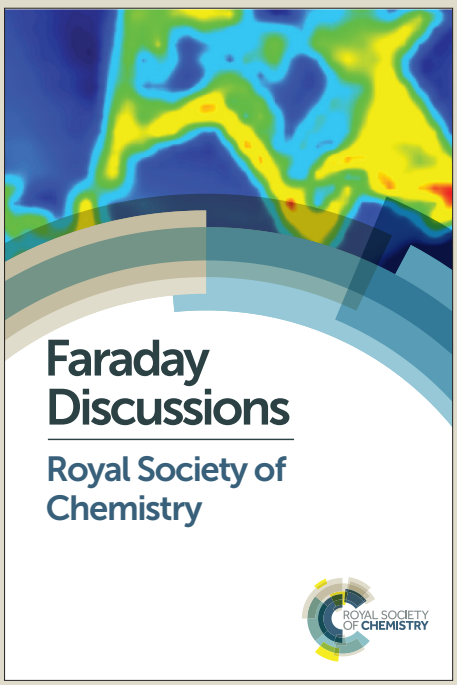

This is an *Accepted Manuscript*, which has been through the Royal Society of Chemistry peer review process and has been accepted for publication.

Accepted Manuscripts are published online shortly after acceptance, before technical editing, formatting and proof reading. Using this free service, authors can make their results available to the community, in citable form, before we publish the edited article. We will replace this *Accepted Manuscript* with the edited and formatted *Advance Article* as soon as it is available.

You can find more information about *Accepted Manuscripts* in the Information for Authors.

Please note that technical editing may introduce minor changes to the text and/or graphics, which may alter content. The journal's standard Terms & Conditions and the Ethical guidelines still apply. In no event shall the Royal Society of Chemistry be held responsible for any errors or omissions in this *Accepted Manuscript* or any consequences arising from the use of any information it contains.

This article can be cited before page numbers have been issued, to do this please use: Y. Odarchenko, D. J. Martin, T. Arnold and A. M. Beale, *Faraday Discuss.*, 2018, DOI: 10.1039/C8FD00007G.

ROYAL SOCIETY OF CHEMISTRY

www.rsc.org/faraday_d

View Article Online
DOI: 10.1039/C8FD00007G

CO oxidation over supported gold nanoparticles as revealed by *operando* grazing incidence X-ray scattering analysis

Yaroslav Odarchenko[a,b], David J. Martin[a,b‡], Thomas Arnold[c,d], Andrew M. Beale[a,b]*

[a] *Department of Chemistry, University College London, 20 Gordon Street, London, WC1H 0AJ, UK*
[b] *Research Complex at Harwell (RCaH), Harwell, Didcot, Oxfordshire OX11 0FA, UK*
[c] *Diamond Light Source, Harwell Science and Innovation Campus, Chilton, Didcot OX11 0DE, UK*
[d] *European Spallation Source ERIC, SE-221 00 Lund, Sweden*
[‡] *Current address: Van't Hoff Institute for Molecular Sciences, University of Amsterdam, Amsterdam, Netherlands, 1098XH*

**corresponding author: Andrew.Beale@ucl.ac.uk*

Keywords: supported gold nanoparticles, CO oxidation, grazing-incidence X-ray scattering, operando

Abstract. The mechanism of carbon monoxide oxidation over gold was explored using a model planar catalyst consisting of monodisperse gold nanoparticles periodically arranged on a single crystal SiO_2/Si(111) substrates using a combination of Grazing Incidence Small Angle X-ray Scattering and Grazing Incidence X-ray Diffraction (GISAXS/GIXD) under reaction conditions. It is shown that nanoparticle composition, size and shape change when the catalyst is exposed to reactive gases. During CO oxidation, the particle's submergence depth with respect to the surface decreases due to the removal of gold oxide at the metal-support edge, meanwhile the particle 'flattens' to maximise the number of the reaction sites along its perimeter. The effect of the CO concentration on the catalyst structure is also discussed. Our results support the dual catalytic sites mechanism whereby CO is activated on the gold surface whereas molecular oxygen is dissociating at the gold-support interface.

Introduction.

In recent decades supported gold nanoparticles (NPs) have received considerable attention in the field of heterogeneous catalysis due to their extraordinary catalytic performance.[1–4] When confined at the nanoscale/atomic level and stabilised on various oxide supports, Au ceases to be inert, and instead becomes a catalyst of choice for many industrially important reactions including acetylene hydrochlorination[1], CO oxidation[4,5] and selective hydrogenation[6,7]. Although the initial discovery of the catalytic activity of Au by Haruta and co-workers was demonstrated for the oxidation of carbon monoxide[4], the nature of the active species, the gold oxidation state and the influence of NP size and shape are not yet well understood despite numerous studies reported in the literature.[8,9]

It is generally agreed that catalytic performance during CO oxidation depends on the nanoparticle size, and the optimal size for the highest turnover frequency was reported to be ~3 nm on titania[10] and alumina[11] supports. However it is challenging to establish a true structure-activity correlation due to the intrinsic complexity of the metal-based heterogeneous catalysts consisting of dispersed Au nanoparticles affixed to the oxide supports such as Al_2O_3, TiO_2 or SiO_2. One of the main reasons is that commonly used preparation methods result in NPs with large particle size distributions (standard deviation, $\sigma >> 1$ nm)[5] or can

View Article Online
DOI: 10.1039/C8FD00007G

yield secondary (and often highly active) sub-nanometer atomic species.[12] Furthermore, in the above studies the catalysts' structure was interrogated before and/or after the reaction that prevents understanding which features are pertinent in a catalytic process.

Recently *operando* 'bulk' techniques (e.g. X-ray absorption spectroscopy, XAS, and powder X-ray diffraction, XRD) have been routinely used to monitor catalytic reactions in real time under industrially relevant conditions, e.g. appropriate pressures and temperatures.[13] However, taking into account that metal loading in the sample is only several percent, the measured signal mainly originates from the *bulk* volume and not from the *surface* where the reaction is happening in the proximity of the NPs.

The importance of *surface* sensitive studies can be emphasised by Grazing-incidence small-angle X-ray scattering (GISAXS) and grazing-incidence X-ray diffraction (GIXD are very powerful techniques for probing the surface of a working catalyst on the macroscopic scale.[7,14] Beale and co-workers studied the hydrogenation of 1,3-butadiene over gold catalysts using *operando* GISAXS/GIXD and demonstrated that the composition and shape of the NPs depends very much on the chemical environment. The particles were shown to be dynamic; undergoing reversible size and shape change during catalytic reaction, highlighting a dynamism often not observed by using bulk analytical techniques.[7] Laoufi *et al*. prepared model Au catalysts on single crystal TiO_2 (110) by chemical vapour deposition and showed that a NP size of 2.1 nm yields a maximum conversion of CO to CO_2.[14] Despite the extreme sintering under reactive gases, the reported size is somehow smaller than the previously published 3 nm for bulk catalysts. The authors didn't discuss the presence of the gold oxide known to form at the metal-support interface[15] and its role in the reaction mechanism. Possibly due to the fact, that only GISAXS analysis was performed, hence only providing information about the particles shape and size. However, it is possible to utilise complementary GIXD studies to identify phase composition, crystal sizes and imperfections.

Thus, a highly controlled synthesis method together with an advanced surface sensitive X-ray analysis can offer the solution to the limitations described above that originate from either the preparation methods used for 'real' catalysts or a conventional bulk analytical methods. By following this strategy we combine the reverse polymer micelle synthesis pioneered by Spatz and co-workers[16] offering tight control over NP size and encapsulation of the free metal species to fabricate supported monodisperse Au NPs regularly patterned on flat single crystal substrates and perform *operando* GISAXS/GIXD analysis during CO oxidation reaction. This unique approach provides insight into the surface-related mechanism and the nature of the active species during this important catalytic process and could help to design a better nanoparticulate catalytic systems with specific NP size and shape.

Materials and Method.

Nanoparticles synthesis. Au nanoparticles with regular periodicity (δ) and particle size of 9.0 ± 0.9 nm were prepared using the reverse micelle method.[16] Block-copolymer PS-b-P2VP (Polymer Source Inc.) was dispersed in toluene (Riedel de Haën, 99.5%) at a concentration of 5 mg/ml, and stirred for one week to achieve complete dissolution. Subsequently, chloroauric acid ($HAuCl_4 \cdot H_2O$, Sigma-Aldrich, 99.999%) was added to the micelle-toluene solution. The metal loading took place in a nitrogen-filled glovebox with relative humidity below 10% to avoid phase separation. This final solution was stirred for another week and then filtered through a 1 μm (Glass Fibre GF100/25) and 2 μm filter (PTFE O-20/25), both from Macherey Nagel, to remove any polymer aggregates.

Catalyst preparation. Model catalysts were prepared by depositing AuNPs on the flat single crystal SiO_2/Si(111) substrate. Silicon wafers (1 cm^2, n-type) were cleaned and subsequently dip coated at a withdrawal rate of 10 mm/min. The dried silicon substrates were then plasma etched using a custom built high vacuum radio frequency oxygen plasma device. An oxygen

View Article Online
DOI: 10.1039/C8FD00007G

plasma was applied for 30 minutes at a power of 50 W, using a chamber pressure of 1.2×10^{-2} mbar. The sample was simultaneously heated on the stage; 50 °C for the first 5 minutes, and then 300 °C for the remaining 25 mins. These 1 cm^2 flat silicon substrates with patterned arrays of Au NPs were then subsequently analysed using GISAXS/GIXD under operando conditions for carbon monoxide oxidation by oxygen.

Grazing incidence small-angle X-ray scattering (GISAXS) and X-ray diffraction (GIXD). *Operando* GISAXS and GIXD experiments were conducted at the I07 beamline, Diamond Light Source, with a configuration similar to that previously used by Arnold *et al*.[17] The photon energy was 10 keV. The focused beam of ca. 0.3×0.3 mm^2 was directed on the sample at an incident angle α of 0.2°. The sample to detector distance (SD) was calibrated using several di□raction orders of Ag behenate. The modulus of the scattering vector $\boldsymbol{q}$ was calculated as $q = 4\pi sin\,\theta/\lambda$, where θ is the Bragg angle and λ - the wavelength of the photons. GISAXS data was collected using a large area detector (Pilatus 2M, 172×172 μm^2 pixel size, 1673×1475 pixels) at a distance of 2685 mm. GIXD was measured using a small swing arm area detector (Pilatus 100K, 172×172 μm^2 pixel size, 487×195 pixels).

The samples were positioned inside a sealed reactor complete with low X-ray absorption mica windows equipped with a computer controlled heating stage (Figure S1). The reactor was connected to a purpose built gas delivery system comprising of switching valves and mass flow controllers which enabled complete control of gas mixing and flow rates. The exit of the reactor was coupled to a mass spectrometer (Pfeiffer, Quadstar 422). GISAXS/GIXD were recorded at different gas compositions and temperature of 573 K. The order was as follows: calcination in O_2 (20% in He) at 573K at flow rate 100 ml/min; He at flow rate 54 ml/min; CO (10% in He) and O_2 (20% in He) at flow rate ratio 36/18 ml/min; CO (10% in He), O_2 (20% in He) and He at flow rate ratio 36/9/9 ml/min; and then clean catalyst afterwards with He gas at 54 ml/min. Carbon dioxide CO_2 was verified as catalytic product using online mass spectrometry (MS). At each step, the waiting time was at least 10 min before collecting the data. The data reduction was performed using the 'DAWN Science' software package.[18] Reduced 1D-GIXD profiles were fitted using Voigt function in the OriginPro 2016 and visualised in Igor Pro.

GISAXS data analysis. The GISAXS data were fitted using the recently developed BornAgain v1.9 software.[19] Being inspired by isGISAXS tool[20], this package gives a possibility to fit the full 2D image using the user built model[21]. A model consisting of Au hemispheres supported on the flat support is a very plausible representation of the 2D catalyst that was successfully used in our previous study on the C_4H_6 hydrogenation.[7] Although the structural changes deduced from the GISAXS analysis were confirmed by the X-ray diffraction and spectroscopy data,[7] in this work we have constructed the model that should better describe our catalytic system. The new model consists of the spheres with bimodal composition submerged into SiO_2/Si(111) substrate that form the hexagonal superlattice (for details see Figure S2). The height H of each particle above the support limits the amount of metallic gold, whereas the depth of submergence, $D=2\cdot R-H$, where R is NP radius, determines the amount of gold oxide phase in each particle. The initial input values for R and D parameters were taken from the microscopy data (Figure S2 in ESI from Beale and co-workers[7]).

The scattering cross-section, σ, for the periodically arranged highly monodispersed NPs could be calculated using the Decoupling Approximation for which the position of the particles is independent of their size and the interference function is defined by an effective structural factor calculated for the average nanoparticle size:[22]

$$\frac{d\sigma}{d\Omega}(\boldsymbol{q}) \cong I_d(\boldsymbol{q}) + |\langle F(\boldsymbol{q})\rangle_\alpha|^2 \times S(\boldsymbol{q}) \qquad (1)$$

View Article Online
DOI: 10.1039/C8FD00007G

where Ω is solid angle around (θ, α), $\boldsymbol{q}$ - scattering vector, $I_d(\boldsymbol{q})$ – is the diffuse part of the scatterting which is linked to the disorder of the scattering objects, $F(\boldsymbol{q})$ – form factor of the nanoparticle, $S(\boldsymbol{q})$ – interference function.

To account for multiple reflection-refraction effects on the surface of the flat SiO_2/Si substrate one can use the Distorted Wave Born Approximation (DWBA) framework.[23] The effective form factor with the four terms associated with the different reflection scenarios of incident or scattered beam reads as follows:

$$F\left(\boldsymbol{q}_{xy}, k_z^i, k_z^f\right) = F\left(\boldsymbol{q}_{xy}, k_z^f - k_z^i\right) + r(\alpha_i)F\left(\boldsymbol{q}_{xy}, k_z^f + k_z^i\right) + r\left(\alpha_f\right)F\left(\boldsymbol{q}_{xy}, -k_z^f - k_z^i\right) + r(\alpha_i)r(\alpha_f)F\left(\boldsymbol{q}_{xy}, -k_z^f + k_z^i\right) \quad (2)$$

where q_{xy} is in-plane component of the scattering vector $q_{xy} = \sqrt{q_x^2 + q_y^2}$; ki and kf are the incident and outgoing wavevectors respectively; r(α) – Fresnel reflection coefficient. The refractive indices of SiO_2, Au, Au_2O_3 were taken from the literature.[24]

Atomic Force Microscopy (AFM). AFM measurements of Au NPs supported on Si(111) substrates were recorded under ambient conditions using a Nanoscope IV controller (Bruker Veeco) in tapping mode. Tapping mode Si probes from Nanosensors were used (PPP-NCHR, resonant frequency 330 kHz, spring constant 42 N/m). The AFM images were processed using Gwyddion software.[25]

Catalytic Testing. Complementary catalytic tests were performed in a 9 mm o.d./7 mm i.d. quartz tubular reactor, using three 5x10 mm^2 rectangular substrates of a Au/SiO_2–Si catalyst. The gas composition order was as follows: calcination in O_2 (20% in He) at 573K at flow rate 100 ml/min; He at flow rate 123 ml/min; CO (1% in He) and O_2 (20% in He) at flow rates 120 and 3 ml/min; CO (1% in He), O_2 (20% in He) and He at flow rates 60, 3 and 60 ml/min. The MS data was normalised using He. The output gases were analyzed by MS (Pfeiffer Omnistar).

Results.

***Operando* GISAXS**. The morphological changes during CO oxidation reaction using model planar catalyst were monitored using *operando* GISAXS. The 1D GISAXS patterns before, during CO oxidation at CO to O_2 ratios 1:1 and 2:1, and after the reaction are shown in Figure 1. The in-plane experimental profiles display a number of peaks with the position ratio of $1 : \sqrt{3} : \sqrt{4} : \sqrt{7}$ corresponding to the (10), (11), (20) and (21) reflections of the 2D hexagonal superlattice formed by the Au NPs (Figure 1). Presence of these peaks during all stages of the reaction indicates that there is no sintering or Ostwald ripening (inter-particle effects). This is also supported by the AFM data measured after the reaction and shown in Figure S3.

When the CO is converted to CO_2 over supported gold there is an increase in intensity of (10) reflection that could be associated with the improved scattering density contrast (inset in Figure 1). This could be due to the scattering objects (i.e. nanoparticles) becoming more identical similar to the inverse melting effect[26] or removal of subsurface and metal-oxide interface gold oxide layer and migration of Au to the surface[7,15], or a combination of both. The signal also increases at larger q ('Porod' region) for the in-plane profiles taken under the reaction conditions that could indicate a more abrupt interface between catalyst and gas atmosphere.[27]

In order to extract changes in NPs' shape and phase under reaction conditions the 2D experimental patterns were fitted using the model with bimodal spheres arranged into the planar hexagonal superlattice (Figure S2). Further details regarding GISAXS analysis can be found in the experimental section. As an example, the experimental pattern collected under

View Article Online
DOI: 10.1039/C8FD00007G

reaction conditions at $CO:O_2$ ratio 2:1 and the fitted pattern are compared in Figure 2. The calculated pattern looks very similar to the real data and shows four interference peaks of the hexagonal symmetry with lattice constant of 73.5 ± 5.9 nm that is in a good agreement with the microscopy data (78.8 ± 9.9 nm) reported elsewhere.[7]

Particle size and depth of submergence calculated based on goodness of the fit as a function of gas atmosphere are summarised in Figure 3. Under He flow the extracted NP radius of 4.2 ± 0.3 nm did not change much from the initial value of R = 4.5 ± 0.5 nm measured using SEM.[7] This value only slightly increases during the oxidation of CO as can be seen on Figure 3a. However the depth of submergence (Figure S2) is significantly decreasing from 3.8 ± 0.3 to 2.8 ± 0.2 nm, indicating that the average particle in the array is simultaneously lifted with respect to the support due to the removal of the gold oxide layer at the metal-oxide interface (Figure 3b). Similar results have been reported for CO oxidation over Au/TiO_2 and the butadiene hydrogenation over the same catalyst.[7,14] Decrease of the contact perimeter along the metal-support interface due to the particle lifting is compensated by its flattening and increase in particle's width (Figure 3c). Such behaviour allows the number of reaction sites situated at the perimeter of the Au particles necessary for CO oxidation to be maximised. At the end of the reaction, the gas atmosphere is switched to helium, the NP's depth value of 3.2 ± 0.3 nm suggesting slow recovery to the original state (Figure 3b).

Since gold particles of 9 nm in diameter are highly crystalline, one can complement GISAXS results with the X-ray diffraction on the surface.

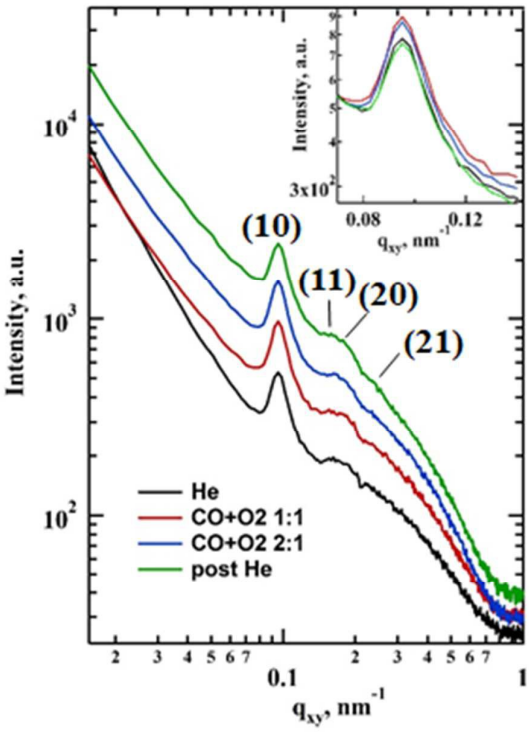

Figure 1. 1D GISAXS in-plane cuts for q_z = 0.339 nm^{-1} showing the signal from the gold nanoparticles hexagonal superlattice with the interparticle distance 76.2 nm. The curves are shifted along Y axis for better visibility.

View Article Online
DOI: 10.1039/C8FD00007G

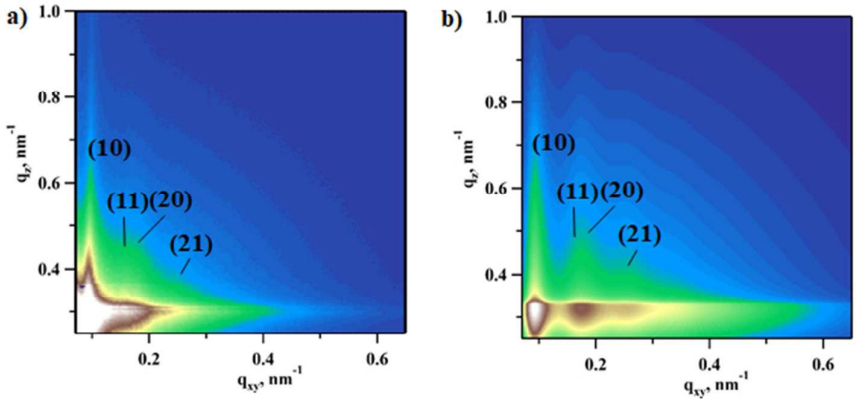

Figure 2. Experimental (a) vs. fitted (b) 2D GISAXS images during carbon monoxide oxidation reaction with CO to O_2 ratio 1:1. Diffuse Kiessig fringes is typical of NP monolayer with the well defined height. The fitting was performed in BornAgain package using bimodal spheres submerged into SiO_2 substrate.

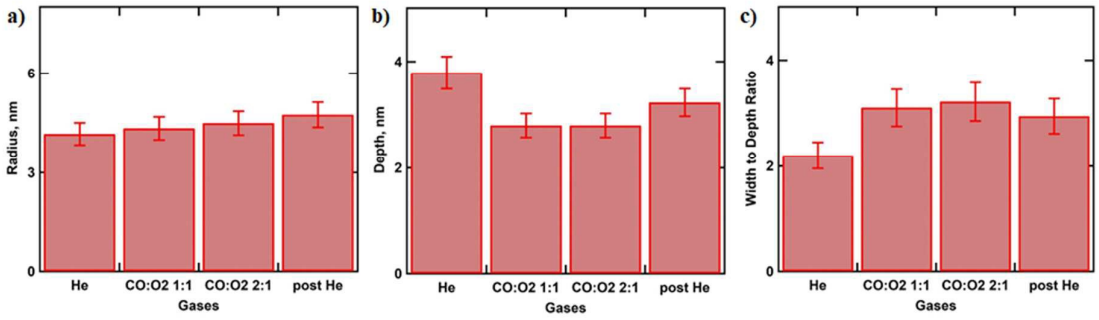

Figure 3. Histogram showing NP radius (a) and depth of submergence (b) with respect to the surface of Au/SiO_2-Si catalyst during CO oxidation calculated from the fitting of the GISAXS images recorded under operando conditions. (c) Histogram displaying calculated width to radius ration under various gas atmospheres.

***Operando* GIXD**. In order to follow the transformations in the crystalline structure of Au NP arrays, the GIXD data was collected under various gas atmospheres (see experimental section for details). Figure 4 shows the 1D GIXD profiles for (110) and (200) reflections of Au fcc lattice.[28] One can see that during exposure to the mixture of CO to O_2 with 2:1 ratio, that corresponds to the optimal stoichiometry for this reaction, both peaks exhibit the largest area. The observed increase in the amount of metallic gold on the catalyst surface can be explained by the intense restructuring at the perimeter of the Au nanoparticle that is triggered by the exothermic reaction of CO oxidation by oxygen and will be discussed later.[29] These results are supported by the GISAXS analysis above showing that the NP's volume buried under the substrate surface is decreasing, corresponding to the removal of Au_2O_3 (Figure 3b).

View Article Online
DOI: 10.1039/C8FD00007G

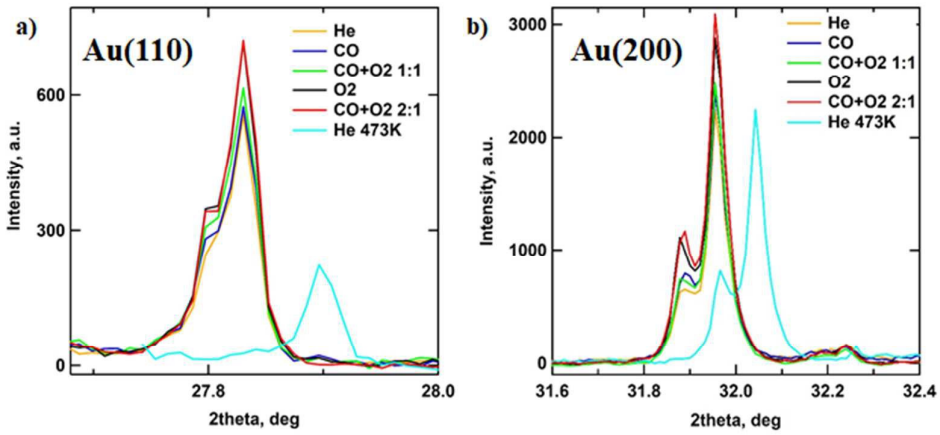

Figure 4. Metallic gold content changes in the Au/SiO_2–Si catalyst during CO oxidation monitored under operando conditions by GIXD. 1D GIWAXS profiles showing the (110) (a) and (200) (b) reflections of Au fcc lattice. All data were collected at 573 K except post He stage (cyan) that T=473 K.

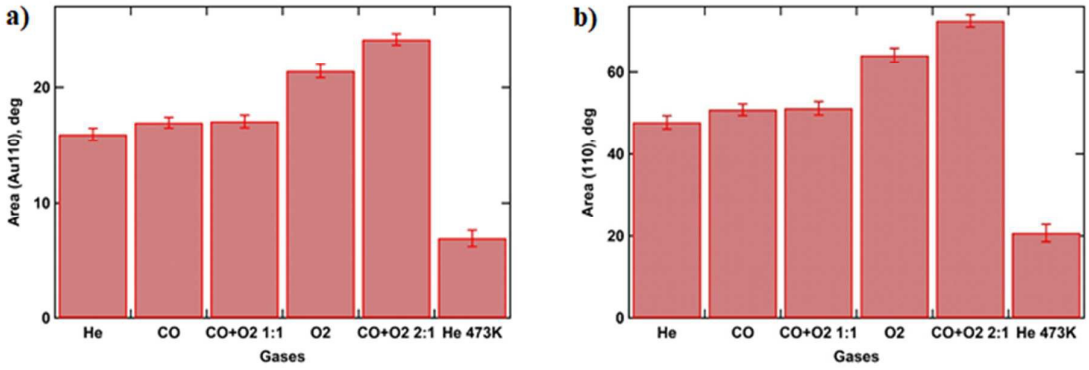

Figure 5. Histograms showing calculated peak areas for Au fcc (110) (a) and (200) (b) reflections under various gas atmospheres, using a Voigt function for peak fitting.

Catalytic data. Figure 6 captures the evolution of mass fragments corresponding to reactants and products during CO oxidation at 573 K. Steps 1 and 2 shows the flow of reactants CO (m/z=28) and O_2 (m/z=32) at ratios 2:1 and 1:1, respectively, via the empty reactor tube. While steps 3 and 4 display reaction stages in the presence of gold catalyst with carbon monoxide to oxygen ratios 1 : 1 and 2 : 1, correspondingly. The increase in CO_2 concentration (m/z=44) during the steps 3, 4 is rather small due to the fact that total mass of the catalyst was in the order of picograms. However the highest CO_2 production rate is achieved at the optimal stoichiometry of carbon monoxide to oxygen that is 2:1. Note this gas composition corresponds to highest degree of gold reduction according to the GISAXS/GIXD data above.

View Article Online
DOI: 10.1039/C8FD00007G

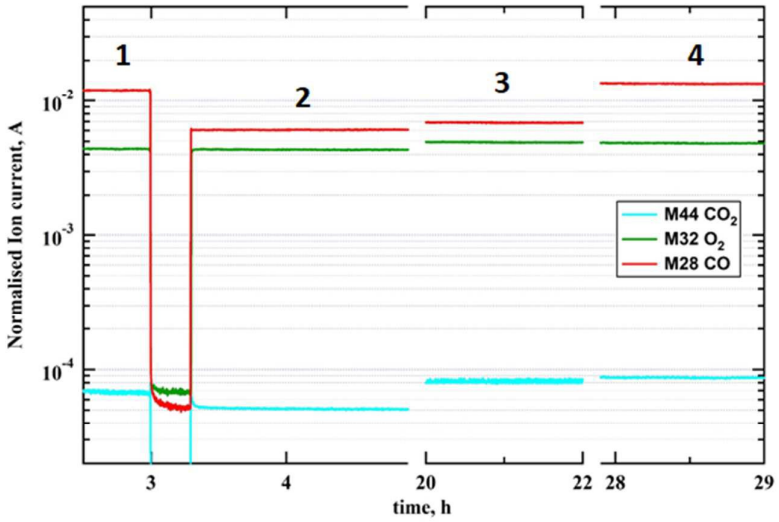

Figure 6. MS data showing production of CO_2 during CO oxidation at 573 K over model planar Au/SiO_2 catalyst. Steps 1 and 4 corresponds to $CO:O_2$ ratio 2:1 without and with catalyst; steps 2 and 3 matches $CO:O_2$ ratio 1:1 without and with catalyst.

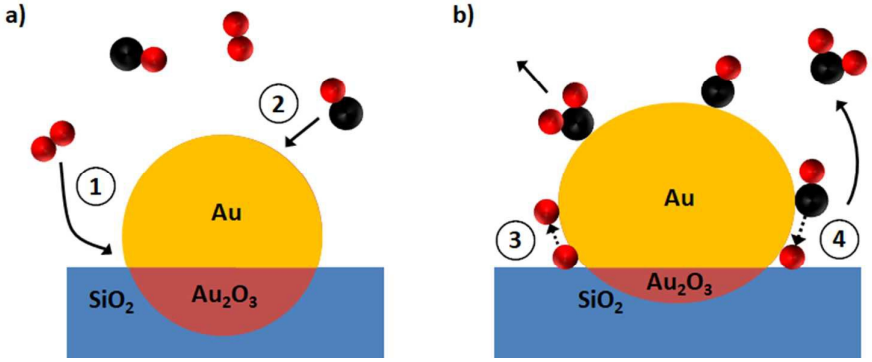

Figure 7. Structural transformations in Au on $SiO_2/Si(111)$ support during CO oxidation as revealed by operando GISAXS/GIXD. (a) Before the reaction (inert gas atmosphere) supported gold nanoparticle represents a bimodal sphere with gold oxide at the gold-substrate interface; (b) during the reaction the gold reduction takes place with the partial removal of the oxide layer as a result the submergence depth decreases whilst particle flattens to maximise its contact perimeter.

Discussion. The observed structural changes and the proposed reaction mechanism are schematically depicted in Figure 7. Initially O_2 from the gas phase is anchored at the perimeter sites (process 1 in Figure 7a) whereas CO is captured preferentially at the gold surface (process 2) as has been shown for Au on SiO_2 catalyst at room temperature.[30] O-O bond scission (process 3) is a next critical step before the CO oxidation reaction. To the best of our knowledge the detailed mechanisms for the process 3 (Figure 7b) were reported only for Au/TiO_2 systems.[9,31] Thus oxygen dissociation could be activated by $CO\text{-}O_2$ complex formation at metal-support interface as observed by Green *et al.*[9] or by Au-OOH species formed near particle perimeter as shown more recently in the work of Saavedra *et al.*[31] who stressed a critical role of support OH groups due to the presence of water. Based on our

View Article Online
DOI: 10.1039/C8FD00007G

findings it is reasonable to assume that oxygen is dissociated over gold on SiO_2 support via the
dual catalytic sites mechanism[9] since the water trap was used in our set-up. Afterwards oxygen atoms react with the adsorbed CO molecules to form CO_2 (process 4 in Figure 7b).
In order to rationalise the observed movement of the gold atoms at the surface and particle-support interface one has to note that the reaction temperature of 573K is above the Hüttig temperature (T_H = 400 K) that allows the surface atoms mobility in metals and is close to the Tammann temperature (T_T = 600 K) that is associated with the solid-state diffusion.[32,33] As CO conversion to CO_2 is strongly exothermic (ΔH=-282.7 kJ/mol)[29], this would further increase temperature at the surface that in turn triggers nanoparticle restructuring.
In our study we show that an increase in the CO pressure accelerates gold reduction that results in the particle size growth and reshaping. Moreover, the increased particle size results in the larger surface area that favours catalyst activity as can be seen in Figure 6. Our findings are in a good agreement with the X-ray photoelectron spectroscopy data and theoretical calculations for gold-based catalysts.[15,34] Cuenya and co-workers reported the decomposition of Au_2O_3 in 5 nm Au NPs supported on SiO_2 in the presence of CO.[15] However their results were based on XPS data, which requires UHV and thus the reaction conditions were not industrially relevant. Ha *et al*. has shown that CO saturation opens fast CO oxidation pathway over Au/CeO_2 system using DFT.[34]

Conclusions.
We have successfully combined a highly controlled synthesis method that yields uniform gold nanoparticles arranged in regular hexagonal arrays with advanced surface-sensitive X-ray scattering techniques to gain insight into the mechanism of CO oxidation, and the role of the metal-support interface. It was revealed that supported Au nanoparticles undergo size and shape transformations during CO oxidation, primarily due to gold oxide removal at the metal-support interface along the particle perimeter. The fact that the highest CO_2 conversion rate corresponds to the catalyst structure with the maximum metallic gold content helps to identify the nature and the origin of the true active species.
We demonstrated that *operando* GISAXS/GIXD studies on model catalysts can be well correlated with the 'real' catalytic systems and thus support the dual catalytic sites mechanism where CO is activated on the gold surface whereas molecular oxygen is dissociating at the gold-support interface.
Our findings also highlight the importance of the *operando* studies in capturing the transient catalyst structures that are often not observed with the conventional methods. Monitoring of the catalyst structure under reaction conditions could help to potentially improve real world catalysts by designing a high surface energy nanodisks or rods that will have better stability and reactivity.

Acknowledgements. The authors would like to thank the EPSRC for funding (grant EP/K007467/1) and the Diamond Light Source for the experiments SI10488 and SI12780. Authors thank Donato Decarolis and Jennifer J. Herbert for help during the beamtime. Dr Jonathan Rawle and Prof Chris Nicklin from I07 beamline, DLS, are also thanked for the excellent technical support. Dr Gennady Pospelov is acknowledged for help in using BornAgain package. The authors are grateful to Prof. Hans-Gerd Boyen (Institute for Materials Research, Hasselt University, Diepenbeek, Belgium) for donation of the Au containing catalyst sample.

References

1 G. Malta, S. A. Kondrat, S. J. Freakley, C. J. Davies, L. Lu, S. Dawson, A. Thetford,

View Article Online
DOI: 10.1039/C8FD00007G

E. K. Gibson, D. J. Morgan, W. Jones, P. P. Wells, P. Johnston, C. R. A. Catlow, C. J. Kiely and G. J. Hutchings, *Science*, 2017, **355**, 1399–1403.
2 A. Corma and H. Garcia, *Chem. Soc. Rev.*, 2008, **37**, 2096.
3 C. Della Pina, E. Falletta, L. Prati and M. Rossi, *Chem. Soc. Rev.*, 2008, **37**, 2077.
4 M. Haruta, T. Kobayashi, H. Sano and N. Yamada, *Chem. Lett.*, 1987, **16**, 405–408.
5 M. Comotti, W.-C. Li, B. Spliethoff and F. Schüth, *J. Am. Chem. Soc.*, 2005, **128**, 917–924.
6 H. Sakurai and M. Haruta, *Catal. Today*, 1996, **29**, 361–365.
7 D. James Martin, D. Decarolis, Y. I. Odarchenko, J. J. J. Herbert, T. Arnold, J. Rawle, C. Nicklin, H.-G. Boyen and A. M. Beale, *Chem. Commun.*, 2017, **53**, 5159–5162.
8 M. C. Kung, R. J. Davis and H. H. Kung, *J. Phys. Chem. C*, 2007, **111**, 11767–11775.
9 I. X. Green, W. Tang, M. Neurock and J. T. Yates, *Science (80-.).*, 2011, **333**, 736–739.
10 G. R. Bamwenda, S. Tsubota, T. Nakamura and M. Haruta, *Catal. Letters*, 1997, **44**, 83–87.
11 J. Jia, K. Haraki, J. N. Kondo, K. Domen and K. Tamaru, *J. Phys. Chem. B*, 2000, **104**, 11153–11156.
12 S. M. Rogers, C. R. A. Catlow, C. E. Chan-Thaw, D. Gianolio, E. K. Gibson, A. L. Gould, N. Jian, A. J. Logsdail, R. E. Palmer, L. Prati, N. Dimitratos, A. Villa and P. P. Wells, *ACS Catal.*, 2015, **5**, 4377–4384.
13 K. Qian, L. Luo, H. Bao, Q. Hua, Z. Jiang and W. Huang, *Catal. Sci. Technol.*, 2013, **3**, 679–687.
14 I. Laoufi, M. C. Saint-Lager, R. Lazzari, J. Jupille, O. Robach, S. Garaudée, G. Cabailh, P. Dolle, H. Cruguel and A. Bailly, *J. Phys. Chem. C*, 2011, **115**, 4673–4679.
15 L. K. Ono, B. R. Cuenya and B. Roldan Cuenya, *J. Phys. Chem. C*, 2008, **112**, 4676–4686.
16 J. P. Spatz, S. Mössmer, C. Hartmann, M. Möller, T. Herzog, M. Krieger, H.-G. Boyen, P. Ziemann and B. Kabius, *Langmuir*, 2000, **16**, 407–415.
17 T. Arnold, C. Nicklin, J. Rawle, J. Sutter, T. Bates, B. Nutter, G. McIntyre and M. Burt, *J. Synchrotron Radiat.*, 2012, **19**, 408–416.
18 M. Basham, J. Filik, M. T. Wharmby, P. C. Y. Chang, B. El Kassaby, M. Gerring, J. Aishima, K. Levik, B. C. A. Pulford, I. Sikharulidze, D. Sneddon, M. Webber, S. S. Dhesi, F. Maccherozzi, O. Svensson, S. Brockhauser, G. Náray and A. W. Ashton, *J. Synchrotron Radiat.*, 2015, **22**, 853–858.
19 J. Burle, C. Durniak, J. M. Fisher, M. Ganeva, G. Pospelov, W. Van Herck and J. Wuttke, 2017.
20 R. Lazzari, *J. Appl. Crystallogr.*, 2002, **35**, 406–421.
21 A. Singh, S. Schipmann, A. Mathur, D. Pal, A. Sengupta, U. Klemradt and S. Chattopadhyay, *Appl. Surf. Sci.*, 2017, **414**, 114–123.
22 M. Kotlarchyk and S. Chen, *J. Chem. Phys.*, 1983, **79**, 2461–2469.
23 S. K. Sinha, E. B. Sirota, S. Garoff and H. B. Stanley, *Phys. Rev. B*, 1988, **38**, 2297–2311.
24 B. L. Henke, E. M. Gullikson and J. C. Davis, *At. Data Nucl. Data Tables*, 1993, **54**, 181–342.
25 D. Nečas and P. Klapetek, *Open Phys.*, 2012, **10**, 181–188.
26 Y. Yu, A. Jain, A. Guillaussier, V. R. Voggu, T. M. Truskett, D.-M. Smilgies and B. A. Korgel, *Faraday Discuss.*, 2015, **181**, 181–192.
27 K. Høydalsvik, J. B. Fløystad, A. Voronov, G. J. B. Voss, M. Esmaeili, J. Kehres, H. Granlund, U. Vainio, J. W. Andreasen, M. Rønning and D. W. Breiby, *J. Phys. Chem. C*, 2014, **118**, 2399–2407.

View Article Online
DOI: 10.1039/C8FD00007G

28 Wyckoff R. W. G., *Crystal Structures,* Interscience Publishers, New York, 2nd Edition., 1963, **1**, 7.
29 T. X. T. Sayle, S. C. Parker and C. R. A. Catlow, *J. Chem. Soc. Chem. Commun.*, 1992, **0**, 977.
30 N. Weiher, E. Bus, L. Delannoy, C. Louis, D. E. Ramaker, J. T. Miller and J. A. van Bokhoven, *J. Catal.*, 2006, **240**, 100–107.
31 J. Saavedra, H. A. Doan, C. J. Pursell and C. Lars, 2014, **345**.
32 J. A. Moulijn, A. E. Van Diepen and F. Kapteijn, *Appl. Catal. A Gen.*, 2001, **212**, 3–16.
33 M. Wolf, H. Kotzé, N. Fischer and M. Claeys, *Faraday Discuss.*, 2017, **197**, 243–268.
34 H. Ha, H. An, M. Yoo, J. Lee and H. Y. Kim, *J. Phys. Chem. C*, 2017, **121**, 26895–26902.